

# Healing of a Topological Scar: Coordination Defects in a Honeycomb Lattice

Benjamin N. Katz\* and Vincent Crespi\*

*Pennsylvania State University*

Received May 31, 2023; E-mail: bnk120@psu.edu; vhc2@psu.edu

**Abstract:** A crystal structure with a point defect typically returns to its ideal local structure upon moving a few bond lengths away from the defect; topological defects such as dislocations or disclinations also heal rapidly in this regard. Here we describe a simple point defect – a two-fold atom incorporated at the growth edge of a 2D hexagonal honeycomb material – whose healing may require a defect complex with 50 or more atoms. *Topologically* the two-fold atom disappears into a single ‘long bond’ between its neighbors, thereby inducing a pentagonal disclination. However, *chemically* this disclination occupies as much physical space as a six-fold ring. This incompatibility of chemistry and topology can cause a “ringing” of the Gaussian curvature that creates an expansive healing region and may even spawn a semi-infinite grain boundary propagating outwards from the topological scar.

Defects in 2D materials<sup>1,2</sup> can be classified by their physical<sup>3</sup>, chemical<sup>4</sup>, or topological character<sup>5,6</sup>. Defects such as Stone-Wales rotations, vacancies, grain boundaries, edge defects, substitutional defects, or chemisorbed species have been studied extensively in systems post-growth<sup>7–10</sup>, but less so as to their ramifications during growth. Here we examine a topological defect – a pentagonal disclination – created by a chemical substitution that changes coordination number, and explore how the chemistry and the topology impose conflicting requirements on how the system heals, i.e. returns to the local bond geometry of the ideal crystal as the system overgrows the defect.

Consider a two-coordinate atom substituted into a three-fold hexagonal honeycomb network. Topologically, this atom disappears into a “long bond” and the ring to which it is bonded becomes topologically five-fold, although it is chemically six-fold. For the system to grow around this **coordination defect** it must repair the topological error while avoiding large deviations in bond geometry, i.e. add one net heptagonal ring to remain asymptotically flat while also bridging the large gap created by the two-fold atom, which generally requires more reach than is provided by a single seven-fold ring.

There are several ways such a system could heal, with different numbers of atoms spanning the gap as depicted in Fig. 1. Attempting to heal with a seven-fold ring immediately above the coordination defect (as would happen in a simple dislocation) produces highly dilated bonds that spontaneously fragment during structural relaxation. Eight-fold and nine-fold rings reduce this bond strain but overscreen the Gaussian curvature of the coordination defect and so require further topological defects to achieve asymptotic planarity. The detailed structural state achieved after this ringing of the Gaussian curvature is our object of study.

If enough two-coordinate impurity atoms are available, then a nine-fold ring above the coordination defect could

hold a second such atom and thus shrink topologically to an eight-fold ring, the two-coordinate atom then templating a second topologically five-fold ring in the next layer to yield the structure shown in the right panel of Fig. 1. This geometry is akin to a graphenic divacancy and has been studied in the context of defects introduced into the interiors of already-grown sheets<sup>10</sup>. However, if the impurity species is rare enough, then a second such atom may not become available before the system overgrows the initial defect. This leaves the left and center panels of Fig. 1 as possible routes for the overgrowth of the coordination defect.

Before moving further, we check if oxygen incorporation on the edge of graphene is favored over attachment to the basal plane to form an epoxide, since oxygen is a prime candidate for a coordination defect in graphene. Density functional theory calculations were performed in VASP<sup>11–14</sup> (with the PBE functional on a  $3 \times 3 \times 1$  k-point grid) to compare the energies of a 72-atom graphene unit cell with two oxygen atoms bound as epoxides to the same sheet with a divacancy that is terminated with two oxygen atoms (effectively replacing a carbon dimer with oxygen atoms). Taking the chemical potential of carbon to be the energy of an atom in the 72-atom bulk graphene layer, these results indicate a preference for oxygen to bind at the graphene edge by 0.94 eV over forming an epoxide.

For simplicity, we model growth on a graphene substrate. The metallic substrates often used experimentally can considerably complicate the edge energetics of *unterminated* graphene sheets through metallic bonding to the sheet edge<sup>15</sup>, so we consider a regime of chemical potential in which the graphene edge is hydrogen-terminated, which weakens this interaction. In any case, many of the reconstructions that may occur at the growth edge for metallic substrates<sup>16,17</sup> are already considered in the branched growth model described below.

Fig. 1 shows our three starting points following incorporation of a two-fold defect in monolayer graphene: an eightfold ring (5\*8\*), a ninefold ring (5\*9\*), or an eightfold ring with a second two-coordinate atom (5\*8\*\*). Each “\*” marks a two-coordinate atom within a ring and the integer just before gives the *topological* size of the ring, not the number of atoms within it. As noted above a 7-fold ring immediately above the coordination defect is not stable. Also, a 10-fold ring is disfavored relative to the 9-fold on energetic grounds. For convenience, we model the two-coordinate atom as a regular carbon atom with two hydrogens attached; this will automatically allow the 8\*\* pathway to be considered on an equal footing with the others through use of a hydrogen chemical potential.

We assume step-flow growth down a zigzag edge, as used previously for modelling chemical vapor deposition on a weakly coupled substrate with low carbon flux<sup>18</sup>. Carbon atoms are added one at a time to flow the step (kink) along the growth edge to form the successive rows

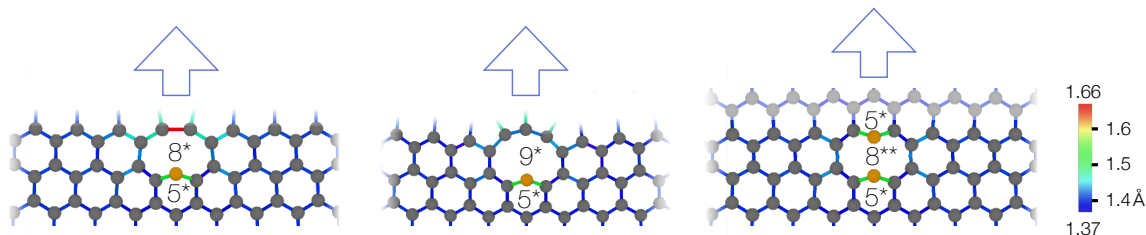


**Figure 1.** Three possible resolutions to the growth beyond a single coordination defect (in orange): the first and second produce an eight-fold or nine-fold ring respectively, while the third has two compensating coordination defects and resolves in a manner similar to a 5/8/5 divacancy structure. Bond lengths are color-coded as indicated in the scale bar at right.

of atoms depicted in alternating light or dark gray in Fig. 2. We assume that carbon atoms already three-fold carbon-coordinate within the bulk of the sheet do not undergo bond breaking and reformation during this process, but carbon atoms at the growth edge may reorganize in the vicinity of each successively added atom.

The initial ( $5^*8^*$ ), ( $5^*9^*$ ), or ( $5^*8^{**}$ ) structures are hydrogen-terminated so that all carbon atoms (other than the coordination defect) are three-coordinate. At this stage the ( $5^*9^*$ ) and ( $5^*8^{**}$ ) pathways are identical; they are only distinguished in the growth of the next row. We simulate the kink-flow growth of at least two additional layers across a branched tree of possible structural outcomes, terminating the highest-energy branches and allowing reconstructions of already-formed rings just behind the kink as it overgrows the coordination defect. We initiate the kink two six-fold rings to the side of the coordination defect, following the numbered atoms of Fig. 3. Each added carbon atom can: (1) attach at the edge of the kink, becoming one-coordinate (or completing a ring and becoming two-coordinate); (2) attach to a one-coordinate atom with both becoming two-coordinate and thus completing a ring; or (3) insert into either of the two most recently completed rings. One- or two-coordinate here refers to the number of carbon neighbors.

We permit the addition of non-six-fold rings so long as they do not worsen the net Gaussian curvature deviation of the prior layer. For example, we permit five-fold rings in the next layer of ( $5^*9^*$ ), but no rings larger than six-fold. We do not allow four-fold or three-fold rings. If the new atom attaches at the edge of the kink, its attachment point is presumed to be the two-coordinate atom nearest the three-coordinate bulk. After this atom is added, we additionally allow one carbon atom (and the associated hydrogen) to move between the two most recently completed rings, shrinking one and growing the other. Any carbon atoms with less than three bonds are then singly terminated with hydrogen and the resulting structure is structurally relaxed. As these structures may have differing hydrogen counts, we balance them with a hydrogen chemical potential taken for growth at 1000 °C and  $10^2$  torr hydrogen partial pressure, which is on the high side of the range (roughly  $10^0$  to  $10^2$  torr) expected to produce hydrogen-terminated graphene in experiment<sup>15</sup> (see Supporting Information). This chemical potential disfavors double hydrogen termination. We thus assume single termination during growth, excepting the 2-coordinate defects added by fiat.

Any structure whose relaxed energy is more than 10 eV above the lowest-energy structure of that step is pruned from the tree, while the remaining branches accrete additional carbon atoms as described above. This process continues until we complete the ring that is as far from

the coordination defect at the one which began that row. The row is then finished with six-fold rings (without reconstructions) for all remaining branches that are within 3.5 eV of the lowest-energy branch. The various outcomes may differ in carbon count as well as hydrogen count. The carbon chemical potential is set to the average addition energy for a pair of carbon atoms to a kink on a pristine graphene edge. The branched tree does not reconstruct the interior of already-formed material (i.e. no Stone-Wales transformations or vacancy formation). By adding carbon atoms singly, it also captures almost all processes that may add carbon atoms in pairs, missing only “dangling dimers”.

The energetics are modelled with the 2013 ReaxFF potential of Srinivasan et al.<sup>19</sup> as implemented in the Large-scale Atomic/Molecular Massively Parallel Simulator (LAMMPS)<sup>20</sup>, as it has previously been used to examine energetics and dynamics of highly defective carbon structures<sup>21–26</sup>. The coordination defect starts at the edge of a graphene flake approximately 30 nm wide along the growth edge and 40 nm deep at the start of growth. It is supported on a fixed graphene substrate and singly terminated by hydrogen on the exposed edges. The structural relaxation at each stage of the branched tree follows a multistep procedure that facilitates optimization of both fast and slow degrees of freedom. Relaxation begins with a 10 fs simulation using a bonded potential with distance-limited dynamics to remove any artifactual strain that may have been created upon introducing the new atoms. We then transition to the REAXX potential. A short series of conjugate-gradient relaxations is followed by a two-stage thermal anneal from 500 to 50 K and then from 50 to 0.1 K, each stage lasting 10 ps. This brief anneal facilitates the relaxation of slow long-wavelength degrees of freedom. The terminating hydrogens buckle slightly out of the plane of the sheet and neither conjugate gradient nor damped dynamics can efficiently find their global energy minimum, creating a jitter of a few tenths of an eV across the entire system. Therefore two successive 50 ps damped-dynamics minimizations are followed by a final conjugate-gradient minimization, sampling the energy every 0.1 ps throughout this process; the lowest energy from this sampling is taken as the minimized energy of the structure at a  $\sim 0.1$  eV resolution.

The energies of these three growth paths are compared in Fig. 3 for the first row of growth, with images and energies of each stage provided in the supporting information. Each free energy is given as a range, the upper and lower bounds of which are determined by the bounds on hydrogen partial pressure for the growth of hydrogen-terminated graphene at 1000 °C, as discussed in Zhang et al.<sup>15</sup>. While the  $5^*9^*5^4$  pathway (now extending the pathway names to include the ring structure of the next row) has an unusually large

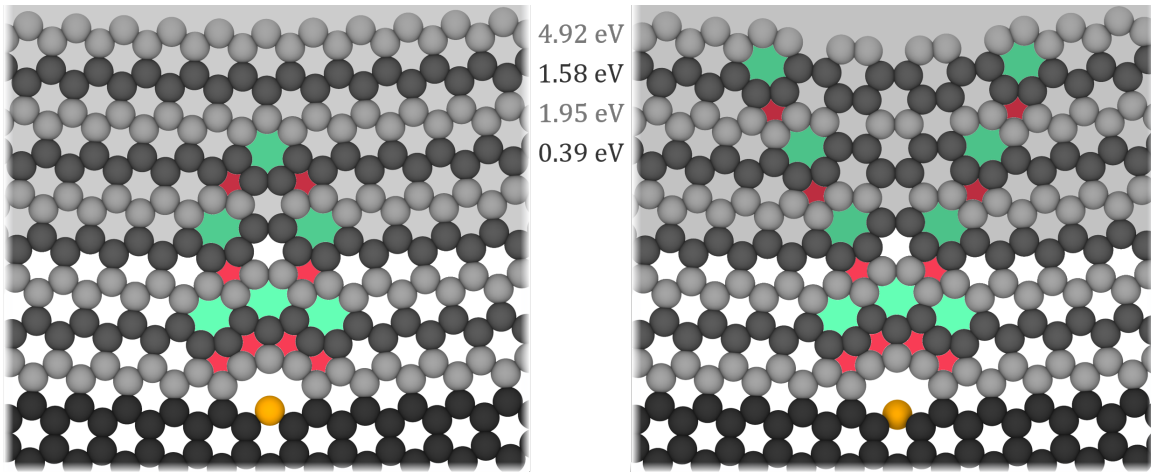


**Figure 2.** Resolution of the growth pathway beginning as  $5^*9^*5^4$ . Successive rows are colored in alternating shades of gray, and non-six-fold rings are colored red (pentagons) and teal (heptagons). The first three rows past the coordination defect (colored orange here) are added according to the algorithm described in the main text; later rows with gray background are added through energetic comparison of various completed rows. Numerical values at center give, row-by-row, the energy by which the structure of the right exceeds that of the structure on the left. In the right panel the defect complex spawns a grain boundary; in the left panel it forms a dislocation.

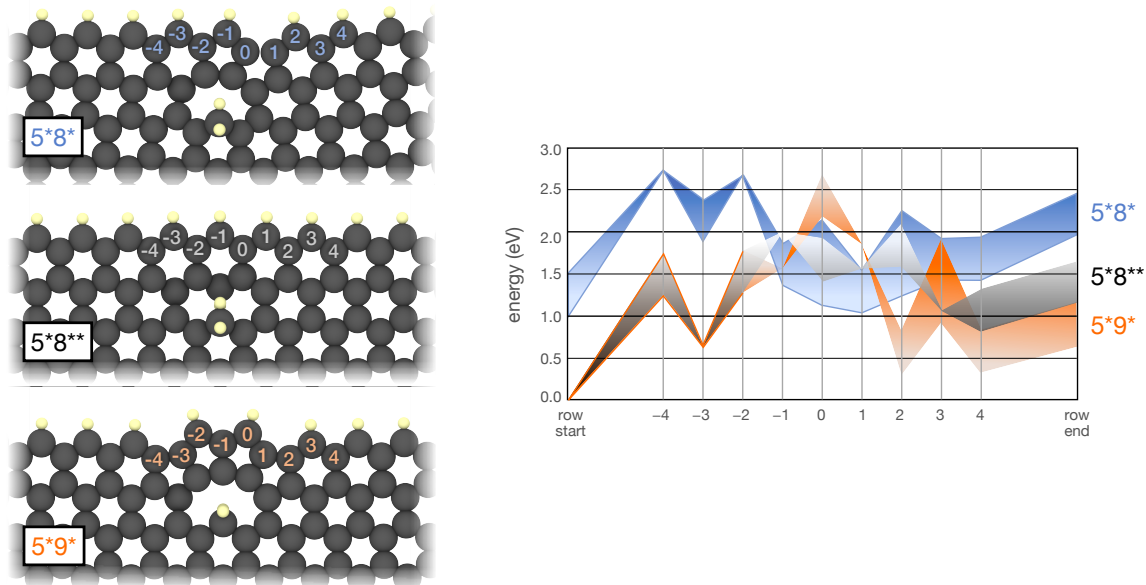


**Figure 3.** Comparative step-by-step energetics for growth of two rows past a coordination defect, resulting in the three outcomes depicted at left. The atoms added are numbered in order of the direction of growth (actual structures at these stages are given in Supporting Information). As the intermediate structures differ in the number of hydrogen atoms, the graphs are broadened to cover a range of hydrogen partial pressures from  $10^2$  to  $10^0$  torr, fading towards the higher partial pressures (which are the lower hydrogen chemical potentials).

number of five-fold rings—two more than required to retain planarity—it nonetheless is the most favorable structure across most of the growth steps. The two steps for which it is not the most favorable (numbered 0 and 1 in Fig. 3) would require multiple ring-opening reconstructions behind or underneath the growth edge to switch to a different pathway. As the free energy gained in such a switch would be comparable to the formation energy of other common defects in graphene, this suggests that  $5^*9^*5^4$  is a viable—if not unique—pathway.

The  $(5^*8^{**}5^*)$  defect is fully healed (i.e. attains zero net gaussian curvature) after addition of a single row, while one of the two five-fold defects added in growth over the  $(5^*8^*5^2)$  defect disappears upon addition of another row. These two structures should then grow further through only

the addition of six-fold rings, yielding a fairly small overall point defect complex. The  $(5^*9^*)$  defect, on the other hand, has over-screened the Gaussian curvature by two pentagons and so we propagate it for a third row, after which it has a one-heptagon excess (Fig. 2). As the curvature excess is now only a single ring, further growth is performed row-by-row, considering patterns of compensatory defect rings adjacent or near-adjacent to defect rings in the prior row, until the structure fully heals. This row-by-row method successfully reproduces the outcomes of the more detailed algorithm for all prior rows and is more computationally efficient.

This defect takes *four* further rows to heal, seven total rows beyond the original defect. The entire seven-row superstructure with fourteen non-sixfold rings that grew above the two-fold coordination defect (shown in Fig. 2

on the left), acts topologically as a single heptagon. The final “topological scar” is thus a very large dislocation. The  $5 \times 8$  pathway grown to similar size would be much lower in energy, but that pathway cannot be easily recovered after the first row of  $5 \times 9 \times 5^4$  has formed: the road to hell is paved with good intentions. This road may even fork into the pair of grain boundaries shown on the right-hand side of Fig. 2, a structure whose row-by-row energies are compared to the  $5 \times 9 \times 5^4$  pathway the left-hand panel in the figure. This suggests that two-coordinate impurities such as oxygen may nucleate grain boundaries in honeycomb lattices.

Although point defects such as substitutions are commonly quite small, we have shown how they need not remain so, if they introduce topological complications into growth around the defect. As the coordination defects studied here can be compensated by a complementary such defect (formed by incorporating a carbon atom that is two-fold coordinate to hydrogen, as in  $5 \times 8 \times 5^*$ ), the formation of *isolated* coordination defects may be favored under conditions that disfavor edge termination by hydrogen or similar species. Graphene is frequently grown under such conditions<sup>15</sup>. In such a situation the  $5 \times 8$  resolution is less accessible and any trace oxygen may then produce the much larger  $5 \times 9 \times 5^4$  defect complex. Here we describe a microscopic mechanism by which this outcome could be much more disruptive to growth than previously imagined, thus providing further motivation to exclude two-coordinate atoms from the growth chamber when pursuing defect-free growth. Alternatively, these large coordination defects may be useful when particular defective morphologies are desired for e.g. gas adsorption or catalysis. Note that our finite simulation size with free boundaries may favor the resolution of  $5 \times 9 \times 5^4$  as a dislocation rather than a grain boundary; in a real system a grain boundary may be more compatible with the elastic relaxation of the sheet and the maintenance of favorable sheet/substrate interactions. More refined control of the density and placement of coordination defects may allow further tuning of sheet morphology, such as the controlled placement of grain boundaries or the modulation of nanoporous geometries.

**Acknowledgement** This work was supported by NSF grants NRT-DESE-1147985 and DMR-2011839. Visualisations were made with the free version of OVITO<sup>27</sup>. Computations for this research were performed on the Pennsylvania State University’s Institute for Computational and Data Sciences’ Roar supercomputer.

## References

- (1) Zou, X.; Yakobson, B. I. *2D Materials*; Cambridge University Press, 2017; pp 359–378.
- (2) Komsa, H.-P.; Krasheninnikov, A. V. *Defects in Two-Dimensional Materials*; Elsevier, 2022; pp 7–41.
- (3) Wu, Z.; Ni, Z. Spectroscopic investigation of defects in two-dimensional materials. *Nanophotonics* **2017**, *6*, 1219–1237.
- (4) Khossossi, N.; Singh, D.; Ainane, A.; Ahuja, R. Recent progress of defect chemistry on 2D materials for advanced battery anodes. *Chemistry – An Asian Journal* **2020**, *15*, 3390–3404.
- (5) Yazyev, O. V.; Louie, S. G. Topological defects in graphene: Dislocations and grain boundaries. *Physical Review B* **2010**, *81*, 195420.
- (6) Popov, I.; Đurišić, I.; Belić, M. R. Designing topological defects in 2D materials using scanning probe microscopy and a self-healing mechanism: a density functional-based molecular dynamics study. *Nanotechnology* **2017**, *28*, 495706.
- (7) Pantelides, S. T.; Puzyrev, Y.; Tsetseris, L.; Wang, B. Defects and doping and their role in functionalizing graphene. *MRS Bulletin* **2012**, *37*, 1187–1194.
- (8) Banhart, F.; Kotakoski, J.; Krasheninnikov, A. V. Structural Defects in Graphene. *ACS Nano* **2010**, *5*, 26–41.
- (9) Boukhvalov, D. W.; Katsnelson, M. I. Chemical

- Functionalization of Graphene with Defects. *Nano Letters* **2008**, *8*, 4373–4379.
- (10) Hofer, C.; Skákalová, V.; Görlich, T.; Tripathi, M.; Mittelberger, A.; Mangler, C.; Monazam, M. R. A.; Susi, T.; Kotakoski, J.; Meyer, J. C. Direct imaging of light-element impurities in graphene reveals triple-coordinated oxygen. *Nature Communications* **2019**, *10*.
- (11) Kresse, G.; Hafner, J. *Ab initio* molecular dynamics for liquid metals. *Physical Review B* **1993**, *47*, 558–561.
- (12) Kresse, G.; Furthmüller, J. Efficiency of *ab-initio* total energy calculations for metals and semiconductors using a plane-wave basis set. *Computational Materials Science* **1996**, *6*, 15–50.
- (13) Kresse, G.; Furthmüller, J. Efficient iterative schemes for *ab initio* total-energy calculations using a plane-wave basis set. *Physical Review B* **1996**, *54*, 11169–11186.
- (14) Kresse, G.; Joubert, D. From ultrasoft pseudopotentials to the projector augmented-wave method. *Physical Review B* **1999**, *59*, 1758–1775.
- (15) Zhang, X.; Wang, L.; Xin, J.; Yakobson, B. I.; Ding, F. Role of Hydrogen in Graphene Chemical Vapor Deposition Growth on a Copper Surface. *Journal of the American Chemical Society* **2014**, *136*, 3040–3047.
- (16) Wang, L.; Zhang, X.; Chan, H. L.; Yan, F.; Ding, F. Formation and Healing of Vacancies in Graphene Chemical Vapor Deposition (CVD) Growth. *Journal of the American Chemical Society* **2013**, *135*, 4476–4482.
- (17) Lee, H. C.; Bong, H.; Yoo, M. S.; Jo, M.; Cho, K. Copper-Vapor-Assisted Growth and Defect-Healing of Graphene on Copper Surfaces. *Small* **2018**, *14*, 1801181.
- (18) Luo, Z.; Kim, S.; Kawamoto, N.; Rappe, A. M.; Johnson, A. T. C. Growth Mechanism of Hexagonal-Shape Graphene Flakes with Zigzag Edges. *ACS Nano* **2011**, *5*, 9154–9160.
- (19) Srinivasan, S. G.; van Duin, A. C. T.; Ganesh, P. Development of a ReaxFF Potential for Carbon Condensed Phases and Its Application to the Thermal Fragmentation of a Large Fullerene. *The Journal of Physical Chemistry A* **2015**, *119*, 571–580.
- (20) Plimpton, S. Fast Parallel Algorithms for Short-Range Molecular Dynamics. *Journal of Computational Physics* **1995**, *117*, 1–19.
- (21) Kroes, J. M. H.; Pietrucci, F.; van Duin, A. C. T.; Andreoni, W. Atom Vacancies on a Carbon Nanotube: To What Extent Can We Simulate their Effects? *Journal of Chemical Theory and Computation* **2015**, *11*, 3393–3400.
- (22) Jensen, B. D.; Wise, K. E.; Odegard, G. M. Simulation of the Elastic and Ultimate Tensile Properties of Diamond, Graphene, Carbon Nanotubes, and Amorphous Carbon Using a Revised ReaxFF Parametrization. *The Journal of Physical Chemistry A* **2015**, *119*, 9710–9721.
- (23) Li, K.; Zhang, H.; Li, G.; Zhang, J.; Bouhadja, M.; Liu, Z.; Skelton, A. A.; Barati, M. ReaxFF Molecular Dynamics Simulation for the Graphitization of Amorphous Carbon: A Parametric Study. *Journal of Chemical Theory and Computation* **2018**, *14*, 2322–2331.
- (24) de Sousa, J. M.; Aguiar, A. L.; Girão, E. C.; Fonseca, A. F.; Filho, A. G. S.; Galvao, D. S. Mechanical Properties of Pentagraphene-based Nanotubes: A Molecular Dynamics Study. *MRS Advances* **2018**, *3*, 97–102.
- (25) Roman, R. E.; Kwan, K.; Cranford, S. W. Mechanical Properties and Defect Sensitivity of Diamond Nanothreads. *Nano Letters* **2015**, *15*, 1585–1590.
- (26) Jensen, B. D.; Odegard, G. M.; Kim, J.-W.; Sauti, G.; Siochi, E. J.; Wise, K. E. Simulating the effects of carbon nanotube continuity and interfacial bonding on composite strength and stiffness. *Composites Science and Technology* **2018**,
- (27) Stukowski, A. Visualization and analysis of atomistic simulation data with OVITO—the Open Visualization Tool. *Modelling and Simulation in Materials Science and Engineering* **2009**, *18*, 015012.

# Supporting Information

## I. CHEMICAL POTENTIAL CALCULATIONS

### A. Hydrogen chemical potential

We assume the hydrogen atoms in our system are coming from a reservoir of  $\text{H}_2$  gas. Following along with the methodology of [1], we use the following formula for the hydrogen chemical potential:

$$-2\mu_{\text{H}} = E_{\text{H}_2} - k_B T \ln(Z_{\text{trans}} Z_{\text{rot}} Z_{\text{vib}}) = E_{\text{H}_2} + k_B T \ln\left(\frac{pV_Q}{k_B T}\right) - k_B T \ln Z_{\text{rot}} - k_B T \ln Z_{\text{vib}}$$

where we take the standard form for the translational partition function of an ideal gas. We calculate this at a temperature of 1000 °C and a pressure of  $10^2$  torr, which are conditions within the expected regime for hydrogen-terminated graphene growth [2], giving  $k_B T \ln\left(\frac{pV_Q}{k_B T}\right) = -1.90$  eV. It is computationally intensive to account for the vibrational entropy of hydrogen bound to the sheet, which would be required to accurately compute the vibrational partition function; in addition, the vibrational excitations of  $\text{H}_2$  are high-energy relative to  $k_B T$  and thus not expected to contribute significantly to the chemical potential. We thus neglect the  $\ln Z_{\text{vib}}$  term. The  $Z_{\text{rot}}$  term then becomes

$$Z_{\text{rot}} = \sum_{J=0}^{\infty} g_J e^{-\frac{E_{\text{rot}}(J^2+J)}{kT}} = \sum_{J=0}^{\infty} g_J e^{-\frac{J(J+1)h^2}{2IkT}}$$

For  $\text{H}_2$ ,  $E_{\text{rot}}$ , which is the energy of the lowest fundamental rotation mode, is 7.37 meV. As we are not in the high-temperature limit, so we collect terms until they contribute less than a tenth to the value of  $Z_{\text{rot}}$ . As  $\text{H}_2$  rotation exchanges a single pair of fermions, the overall wavefunction needs to be antisymmetric. Since H has nuclear spin 1/2, for each rotational state w/ quantum number  $J$  there are  $(I+1)(2I+1)$  symmetric functions and  $I(2I+1)$  antisymmetric functions, which yields 3 symmetric and 1 antisymmetric function for  $I = 1/2$ . Functions with odd  $J$  are already antisymmetric and even  $J$  functions are symmetric, so odd  $J$  needs symmetric spin and vice versa. Thus  $Z_{\text{rot}}$  splits into two functions, replacing  $J$  by  $2K$  and  $2K+1$  and including the appropriate degeneracies:

$$Z_{\text{rot}} = \sum_{K=0}^{\infty} (4K+1) e^{-\frac{2(2K+1)E_{\text{rot}}}{kT}} \text{ for even } J,$$

$$Z_{\text{rot}} = \sum_{K=0}^{\infty} 3(4K + 3)e^{-\frac{(2K+1)(2K+2)E_{\text{rot}}}{kT}} \text{ for odd } J$$

and we collect terms in the overall sequence up to  $J = 10$  (so 6 terms in the first sequence and 5 in the second). This gives us a value of  $k_B T \ln(Z_{\text{rot}})$  of 0.361 eV.

As we are simulating the structures in the ReaxFF potential in LAMMPS [3, 4], we calculate the value of  $E_{\text{H}_2}$  in this potential, and so our final value of  $\mu_{\text{H}}$  comes to  $\sim 4.00$  eV, or  $\sim 92.13$  kcal/mol. In the main text we use a range when plotting the free energy along the various growth paths, corresponding to partial pressures from  $10^0$  to  $10^2$  torr.

## II. ENERGY TABLE FOR SECOND LAYER GROWTH

Table I. Table of compared energies (in eV) for the second layer of growth past the defect, as shown in Figure 3 in the main text. These are the energies of the most favorable structure for each growth path at each step: multiple structures were evaluated at each step.

Step	$5^*-8^*-5$	$5^*-9^*-5^4$	$5^*-8^{**}-5^*$
row start	1.50 (-1C,-1H)	0.00 (+0C,+0H)	0.00 (+0C,+0H)
-4	2.74 (+8C,+0H)	1.76 (+9C,+1H)	1.76 (+9C,+1H)
-3	1.88 (+9C,-1H)	0.62 (+10C,+0H)	0.62 (+10C,+0H)
-2	2.68 (+10C,+0H)	1.78 (+11C,+1H)	1.78 (+11C,+1H)
-1	1.36 (+11C,-1H)	1.56 (+12C,+0H)	1.99 (+12C,+0H)
0	1.13 (+12C,-1H)	2.70 (+13C,+1H)	1.93 (+13C,+1H)
1	1.03 (+13C,-1H)	1.86 (+14C,+0H)	1.57 (+14C,+0H)
2	1.23 (+14C,-2H)	0.29 (+15C,-1H)	2.10 (+15C,+1H)
3	1.42 (+15C,-1H)	0.92 (+16C,-2H)	1.05 (+16C,+0H)
4	1.42 (+16C,-1H)	0.32 (+17C,-1H)	1.31 (+17C,+1H)
row end	1.95 (+17C,-1H)	0.65 (+18C,-1H)	1.65 (+17C,+1H)

Energies are set relative to the lowest energy of Step 0. Step 0 is the previous completed row, then Step 1 begins with the addition of several carbons along the undefected region: each step beyond this adds an additional carbon atom (save for the last step, which completes the row): the energy given at each step is that of the lowest-energy structure found for the addition of that carbon.

### III. SIMULATED STRUCTURE POSITIONS AND ENERGIES

#### A. Images of most favorable structures along growth paths

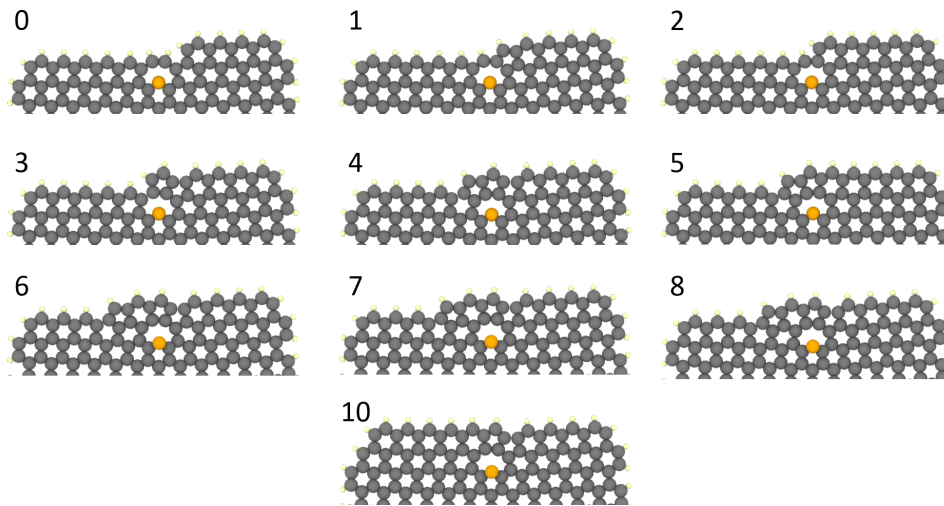


Figure 1. The lowest-energy structure at each step for the  $5 \times 8 \times 5$  growth pathway in the second layer. Steps correspond to the table above; numbers correspond to the step numbers in the position files and energy tables.

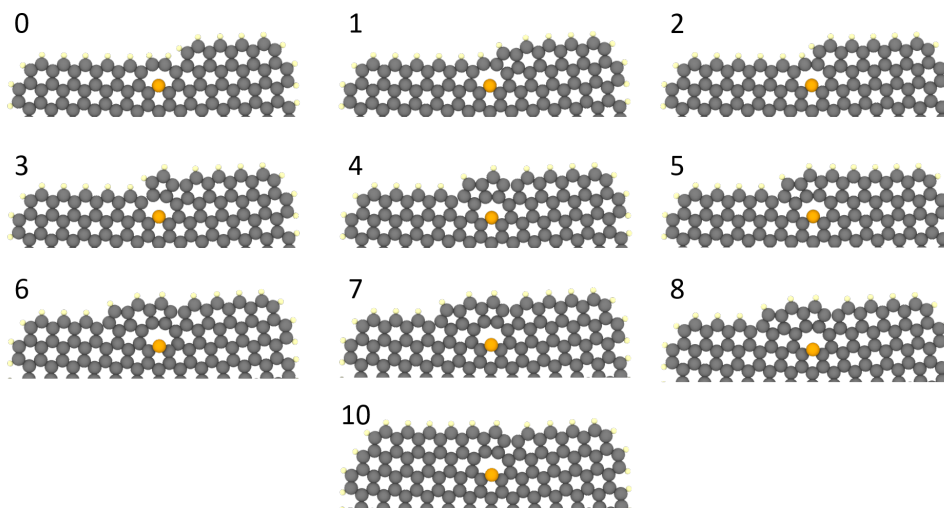


Figure 2. The lowest-energy structure at each step for the  $5 \times 8 \times 5$  growth pathway in the second layer. Steps correspond to the table above; numbers correspond to the step numbers in the position files and energy tables.



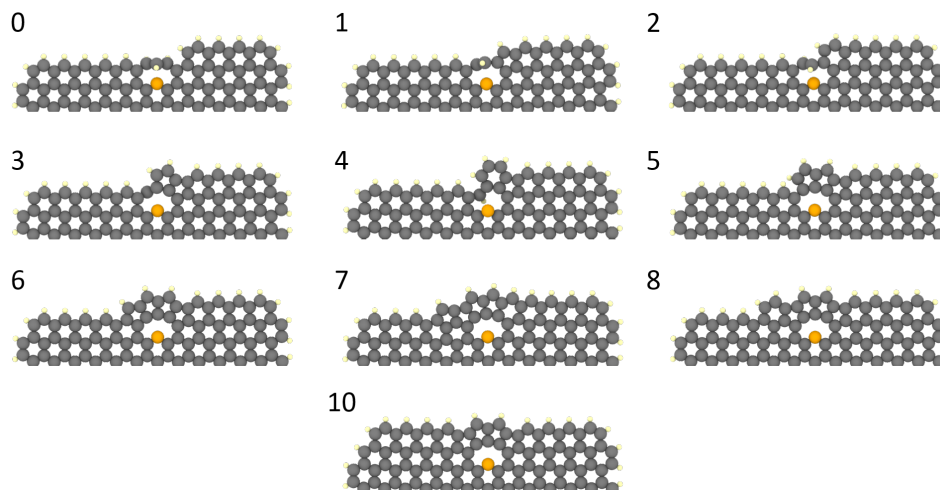


Figure 3. The lowest-energy structure at each step for the  $5 \times 9 \times 5^4$  growth pathway in the second layer. Steps correspond to the table above; numbers correspond to the step numbers in the position files and energy tables.

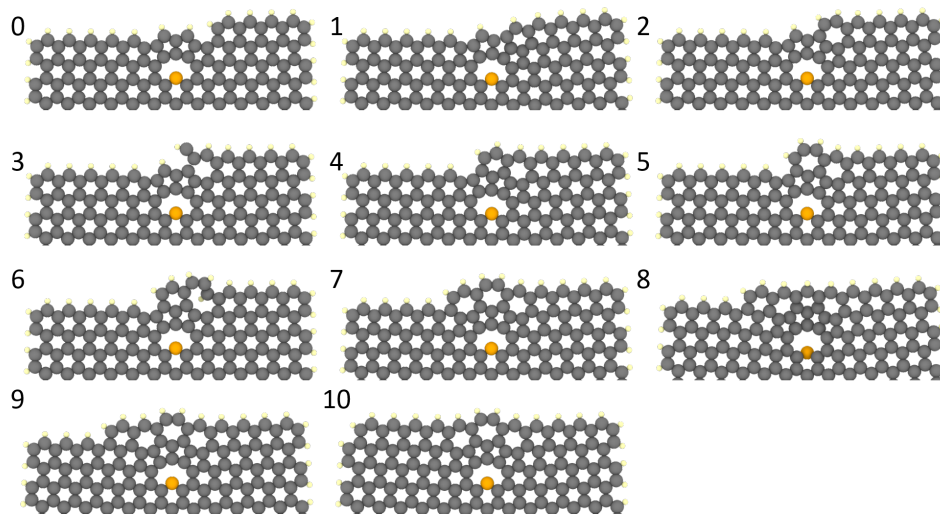


Figure 4. The lowest-energy structure at each step for the  $5 \times 9 \times 5^4$  growth pathway in the third layer. Numbers correspond to the step numbers in the position files and energy tables.

Simulated structure positions (given in LAMMPS dump files) and energies are included in a 7-ZIP file ('simulated\_positions.7z') as part of the Supporting Information. The top-level directory features a folder for the structures in the  $5 \times 8 \times 5$  growth path, divided into folders for the second and third rows, and a folder for the structures in the  $5 \times 8 \times 5^*$  and  $5 \times 9 \times 5^4$  growth paths, divided into folders for the second, third, and succeeding rows. The  $5 \times 8 \times 5^*$

and  $5 \times 9 \times 5^4$  structures are commingled, as they share common structures along the growth pathway. In the top-level directory is also provided a position file for the substrate, which (to save space) is omitted from the position files for all the structures, but was included in the simulation of the structures.

Files containing the energies, and a correspondence table to the structure filenames and their ring counts are also provided, both in a CSV format broken apart into separate files for the  $5 \times 8 \times 5$  growth path, the  $5 \times 8 \times 5^*$  and  $5 \times 9 \times 5^4$  growth paths for the second row, the  $5 \times 9 \times 5^4$  growth path for the third row, and the  $5 \times 9 \times 5^4$  growth path for the rows beyond the third, as well as in an Excel spreadsheet featuring all these growth paths collected (and with functioning formulas to flag viable structures based on their energies).

In the files, the structure ring counts are given in the form ‘A/B/C/D/...’, where A—D are numbers giving the size of rings proceeding from the start of the growth simulation to the current last-formed ring along the direction of growth; for example, ‘6/5/5/7/6’. If a structure includes a ‘+1’ at the end, this indicates a dangling monomer, as in ‘6/5+1’. If a structure includes an added number with ‘\*’ following it (for example, ‘6/6/7/6/6/6+3\*’), this indicates that the last three carbons are nominal, this structure was not simulated, and the energy was obtained by taking the original structure (here ‘6/6/7/6/6/6’) and adding  $3\mu_C$ . In some of the later rows of the  $5 \times 9 \times 5^4$ , different comparison cases feature differing numbers of rings; in that case, to correlate one layer to another absent rings were denoted by ‘X’, as in ‘6/5/X/5/6’.

Movies are also provided for growth across the second layer for the  $5 \times 8 \times 5^*$  and  $5 \times 9 \times 5^4$  paths, and for the third layer for the  $5 \times 9 \times 5^4$  path, showing the best structures at each step. The hydrogen chemical potential used to select these structures is at a lower pressure than the potential used above, so the structures selected are different in a few cases. In addition, a movie is provided that follows the branched-tree algorithm described in the main text, following the growth across the third layer. As the algorithm encounters states that are disallowed by their energy exceeding the permitted limit (which for the movie was chosen to be much lower than for our overall analysis covered in the main text), it backtracks to

the last permitted structure capable of branching.

---

- [1] C. G. V. de Walle and J. Neugebauer, Role of hydrogen in surface reconstructions and growth of GaN, *Journal of Vacuum Science & Technology B: Microelectronics and Nanometer Structures* **20**, 1640 (2002).
- [2] X. Zhang, L. Wang, J. Xin, B. I. Yakobson, and F. Ding, Role of hydrogen in graphene chemical vapor deposition growth on a copper surface, *Journal of the American Chemical Society* **136**, 3040 (2014).
- [3] S. G. Srinivasan, A. C. T. van Duin, and P. Ganesh, Development of a ReaxFF potential for carbon condensed phases and its application to the thermal fragmentation of a large fullerene, *The Journal of Physical Chemistry A* **119**, 571 (2015).
- [4] S. Plimpton, Fast parallel algorithms for short-range molecular dynamics, *Journal of Computational Physics* **117**, 1 (1995).